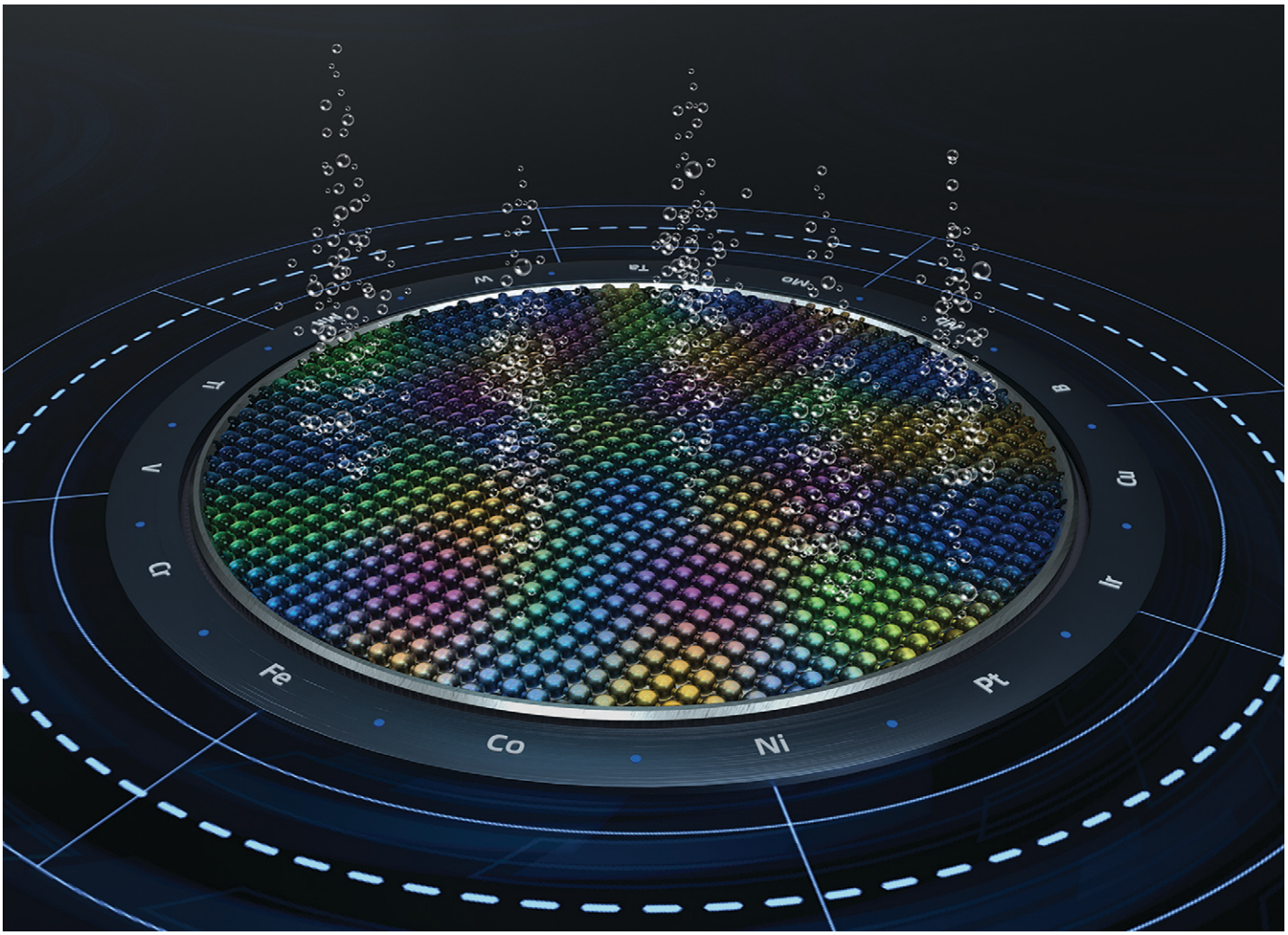

Showcasing research from Professor Huo's laboratory, Ningbo Institute of Materials Technology and Engineering, Chinese Academy of Science, Ningbo, China.

High-throughput bubble screening for rapid design of multi-component alloy catalysts for efficient oxygen evolution

Multicomponent alloys offer a powerful route to break the efficiency limits of the oxygen evolution reaction, but rapidly identifying the optimal composition remains a major challenge. Here, a high-throughput strategy based on oxygen bubble evolution was developed to efficiently screen catalyst activity across complex alloy libraries. Using this method, an Al-Co-Ni-Fe-Mo alloy was optimized and reconstructed into active nanosheet arrays, delivering excellent OER activity and long-term stability, providing a practical pathway toward scalable non-noble-metal catalysts for green hydrogen production.

Image reproduced by permission of Guowei Li, Jun-Qiang Wang, Juntao Huo from *Catal. Sci. Technol.,* 2026, **16**, 3520.

As featured in:

See Guowei Li, Jun-Qiang Wang, Juntao Huo *et al.*, *Catal. Sci. Technol.*, 2026, **16**, 3520.

ROYAL SOCIETY OF CHEMISTRY

rsc.li/catalysis

Registered charity number: 207890

Catalysis Science & Technology

ROYAL SOCIETY OF CHEMISTRY

PAPER

View Article Online
View Journal | View Issue

Cite this: *Catal. Sci. Technol.*, 2026, **16**, 3520

High-throughput bubble screening for rapid design of multi-component alloy catalysts for efficient oxygen evolution

Puchang Hou,[ab] Ruizhe Ru,[b] Ziyong Zhang,[b] Jinyan Xie,[b] Lei Zhang,[b] Fei Han,[b] Guowei Li, *[b] Jun-Qiang Wang *[b] and Juntao Huo *[b]

The sluggish four-electron oxygen evolution reaction (OER) with a high kinetic barrier remains the major bottleneck for industrial alkaline water electrolysis, motivating the development of efficient and durable non-noble metal catalysts. Multicomponent alloying offers a powerful route to tune OER-active sites through inter-element electronic interactions and synergistic redox chemistry. However, the enormous compositional space makes the rational optimization of elemental ratios labor-intensive and scientifically challenging. Here, we establish a product-bubble-based high-throughput screening strategy that directly correlates oxygen bubble evolution behavior with catalytic activity, enabling rapid identification of promising compositions from a continuously varied Al–Co–Ni–Fe–Mo multicomponent alloy library. Guided by this screening, we synthesize the target composition $Al_{32}Co_{37.5}Ni_{8.5}Fe_{10}Mo_{12}$ on nickel foam and further activate it *via* dealloying. Dealloying induces *in situ* reconstruction into vertically aligned nanosheet arrays, selectively leaches Al, enriches Co at the surface, and promotes the formation of high-valence metal species. As a result, the dealloyed sample delivers low overpotentials of 269 mV and 312 mV at 10 and 100 mA cm^{-2} in 1.0 M KOH, respectively, and maintains stable operation at both current densities. This work provides a fast and intuitive pathway for screening and designing non-precious multicomponent OER catalysts with promising potential for practical water electrolysis applications.

Received 11th March 2026,
Accepted 21st April 2026

DOI: 10.1039/d6cy00309e

rsc.li/catalysis

Introduction

The anodic OER is widely recognized as the kinetic bottleneck in alkaline water electrolysis because it proceeds through a multi-step, four-electron/proton-coupled pathway with large activation barriers. Breaking these barriers requires highly active surface sites that can rationally balance the adsorption energies of key intermediates while maintaining rapid charge transfer and efficient gas release.[1–3] Considerable progress has been achieved with metal-based catalysts and simple transition-metal compounds, where operando reconstruction often generates the true active (oxy)hydroxide surface.[4–6] For example, NiFe-layered double hydroxides remain among the most effective non-noble OER catalysts and continue to evolve *via* electronic/morphological engineering to improve activity at practical current densities.[7,8] Perovskite oxides such as BSCF have also demonstrated high intrinsic activity driven by electronic-structure design principles.[9–11] In addition, conductive transition-metal phosphides[12] and sulfides[13] can deliver strong OER performance, but their catalytic behavior is frequently governed by surface oxidation/reconstruction under anodic bias.[14] Despite these advances, further boosting the density and intrinsic activity of catalytic sites, especially under high-current operation, remains a major challenge.[15–19]

Multicomponent alloys[20,21] offer an attractive pathway to surpass the limitations of single-component catalysts because multiple metallic species can cooperatively tune the local electronic structure and adsorption energetics through inter-element charge transfer.[22–24] In practice, this multi-site synergy can create a broader and more continuous distribution of binding energies, improving the probability of forming near-optimal active motifs for the OER while simultaneously enhancing conductivity and mechanical robustness.[25,26] Recent studies on compositionally complex alloys and related multicomponent systems have shown that surface chemistry and oxidation-state regulation (*e.g.*, Co-centered motifs in Fe–Co–Ni-rich matrices) can enhance OER activity and stability.[27] However, the central challenge is compositional design: once four or more components are involved, the combinatorial space of elemental ratios expands dramatically, and small ratio changes can lead to

[a] *School of Materials Science and Chemical Engineering, Ningbo University, Ningbo 315211, China*
[b] *Zhejiang Key Laboratory of Magnetic Materials and Applications, Ningbo Institute of Materials Technology and Engineering, Chinese Academy of Science, Ningbo, Zhejiang 315201, China. E-mail: liguowei@nimte.ac.cn, jqwang@nimte.ac.cn, huojuntao@nimte.ac.cn*

large variations in phase structure, reconstruction behavior, and catalytic performance.[28] As a result, conventional one-composition-at-a-time synthesis and electrochemical testing becomes prohibitively time-consuming and struggles to keep pace with the rapid iteration demanded for modern catalyst discovery and practical performance optimization.[29,30]

High-throughput experimentation (HTE) addresses a basic mismatch in multicomponent catalyst design; specifically, the composition space grows quickly, but conventional synthesis and electrochemical testing proceed one sample at a time.[31–33]

Composition-spread thin-film libraries prepared by co-sputtering provide a practical way to solve this problem because they generate continuous composition gradients on a single substrate while maintaining good uniformity and reproducibility.[34] Once such a library is available, electrochemical mapping tools, including scanning droplet cells, can probe many locations in a short time and produce composition-property maps that highlight trends across the entire space rather than isolated data points.[35,36] Bubble-based screening offers a direct and scalable option for the OER. Under a fixed potential, oxygen generation causes bubbles to nucleate, grow, and detach on the catalyst surface, and these dynamics carry information about the local reaction rate.[37] By recording the bubble evolution using optical imaging and quantifying features such as bubble density and growth behavior over time, one can quickly distinguish more active regions from less active ones across a composition gradient.[38] Prior studies have shown that bubble-derived metrics can track OER activity with good agreement with conventional electrochemical measurements, making bubble screening a useful first-pass filter. This approach is especially suited to the alkaline OER because it monitors the reaction product in real time and can be implemented with simple imaging and analysis, which enable rapid navigation of large multicomponent design spaces, It possesses favorable application potential for electrocatalytic systems featuring distinct bubble generation characteristics.[39,40]

In this work, we use a non-noble five-metal Al–Co–Ni–Fe–Mo system as a model multicomponent alloy platform. By implementing a bubble-based high-throughput screening protocol on a continuously varying composition library, we rapidly locate a high-activity composition region and identify the optimal ratio as $Al_{32}Co_{37.5}Ni_{8.5}Fe_{10}Mo_{12}$. Guided by this screening outcome, we synthesize the target composition on nickel foam and employ a dealloying strategy to trigger *in situ* structural reconstruction, yielding vertically oriented nanosheet arrays with pronounced Al leaching and surface Co enrichment. The resulting catalyst delivers low OER overpotentials of 269 mV at 10 mA cm^{-2} and 312 mV at 100 mA cm^{-2} in 1.0 M KOH, with a Tafel slope of 37.1 mV dec^{-1} and sustains stable operation for 100 h at both current densities. Overall, this study demonstrates a reliable and intuitive route for the rapid screening and design of multicomponent OER catalysts toward practical water electrolysis applications.

Results and discussion

In this work, we used a stepwise process to prepare multicomponent alloy catalysts with controlled composition and structure (Fig. S1). We first fabricated a composition-spread Al–Co–Ni–Fe–Mo thin-film library by multi-target co-sputtering.[41,42] The library was then dealloyed in an alkaline solution to trigger surface reconstruction, after which bubble-based parallel screening was used to rapidly select the most active composition region.[43]

Fig. 1a illustrates the crystal model of the multicomponent alloy. It shows a face-centered cubic (FCC) unit cell, where the five elements occupy the lattice sites in a random manner. The phase structure of the Al–Co–Ni–Fe–Mo library before and after dealloying was examined by XRD (Fig. 1b). The as-deposited library shows three main peaks at 43.6°, 50.8°, and 74.7°, which correspond to the (111), (200), and (220) planes of cubic 3d transition metals (PDF#47-1405).[44] No extra peaks are observed, indicating a single-phase solid solution without obvious impurities. After dealloying, the peaks become slightly stronger and narrower. This suggests improved structural order and reduced microstrain during reconstruction.

SEM images show that the as-deposited library is a smooth and dense film (Fig. 1c and S2). The cross-sectional TEM image (Fig. S3) confirms a uniform thickness with no clear pores. The SAED pattern (Fig. S4) shows diffuse rings, indicating a polycrystalline structure. The HRTEM image reveals lattice fringes with a spacing of 0.207 nm, consistent with the FCC (111) plane. After dealloying in 5 M NaOH for 1 h, the surface is fully transformed into a dense and interconnected nanosheet array (Fig. 1d). This structure increases the accessible surface area and provides open channels for electrolyte transport and oxygen release.[45] The cross-sectional TEM image (Fig. 1e) shows three layers after dealloying: a ~100 nm transition layer, a remaining precursor layer, and a nanosheet layer. EDS results (Fig. S5) show strong Al loss and clear Co enrichment at the nanosheet surface. HRTEM images of the dealloyed layer (Fig. 1f and S6) show nanocrystalline domains with disordered orientations and many defects, such as dislocations and lattice distortion. These results support that dealloying is driven by selective Al dissolution, followed by reorganization of the remaining metals to form the nanosheet framework and enrich active components at the surface.[46,47]

To quickly find the best composition, under strictly controlled experimental conditions, we developed a bubble-based parallel screening method, where the local OER activity is judged from oxygen bubble formation on the catalyst library during electrolysis.[39] By utilizing compositional differences across different regions, this method allows us to compare many compositions on one sample without running full electrochemical tests for each segment, which shortens the screening time (Fig. S7). Before screening, the library was activated by cyclic voltammetry at 50 mV s^{-1} for 20 cycles and then examined by linear sweep voltammetry (LSV) (Fig. S8).

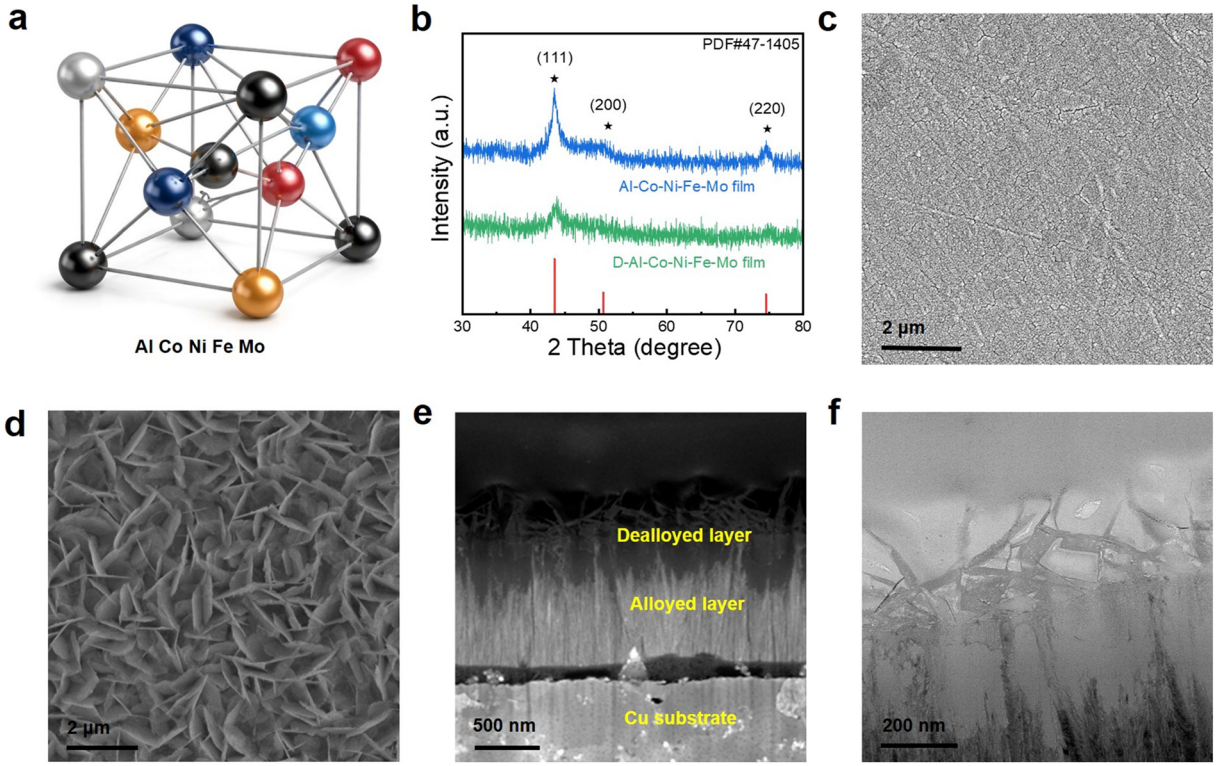

Fig. 1 Structural characterization of the Al–Co–Ni–Fe–Mo library before and after dealloying. (a) Crystal structure model of the multicomponent alloy. (b) XRD patterns of the samples before and after dealloying. (c) SEM image of the as-deposited library. (d) SEM image of the library after dealloying. (e) Cross-sectional TEM image of the dealloyed library. (f) HRTEM image of the dealloyed layer.

We next held the electrode at a constant overpotential of 330 mV and recorded the bubble evolution with time. Under these conditions, bubbles nucleate, grow, merge, and finally detach from the surface (Fig. S9). At the same recording time, different regions of the library showed clear differences in bubble density and bubble growth. Regions with faster bubble nucleation, higher growth rates and denser bubble distribution typically exhibit higher OER activity, as confirmed by follow-up electrochemical tests (Fig. 2b–d). We also tracked bubble nucleation and coalescence at fixed positions to verify that the trend is stable over time (Fig. S10). Based on bubble density and bubble volume, we divided the library into three activity regions: bubble-rich (high activity, Fig. 2b), intermediate (moderate activity, Fig. 2c), and bubble-poor (low activity, Fig. 2d). We divided the sample library into multiple independent analysis regions, calculated and summarized the bubble volume and density of each region, and analyzed the elemental content of each region *via* EDS (Fig. S11). Combining the bubble map with EDS composition analysis gave an activity–composition relationship (Fig. 2a). The most active region corresponds to Al : Co : Ni : Fe : Mo = 32 : 37.5 : 8.5 : 10 : 12 (at%), which was later confirmed by detailed measurements on fixed-composition samples.[48,49]

To confirm that the bubble-based screening gives reliable composition guidance, we prepared two fixed-composition samples using customized sputtering targets taken from the positions marked in Fig. 2b. The first composition is $Al_{32}Co_{37.5}Ni_{8.5}Fe_{10}Mo_{12}$ (denoted as Al_{32}), which lies in the bubble-rich, high-activity region. The second is $Al_{31.5}Co_{37}Ni_{10}Fe_{11}Mo_{10.5}$ (denoted as $Al_{31.5}$),

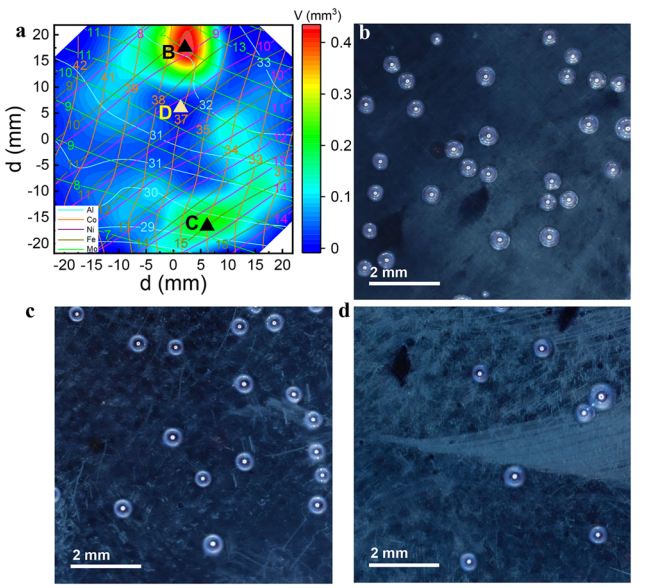

Fig. 2 (a) Contour map of the composition distribution grid and bubble volume distribution. (b) Bubble-rich (high activity, B). (c) Intermediate (moderate activity, C). (d) Bubble-poor (low activity, D).

which lies in a lower-bubble, lower-activity region. According to the screening rule, these two compositions should show clearly different OER performance, so they provide a direct check of the screening result. Before dealloying, the Al_{32} sample forms a dense and smooth alloy film on nickel foam, without any nanosheet features (Fig. S12). The film thickness is about 200 nm. The HRTEM image (Fig. 3b) shows a nanocrystalline structure with short-range order, and the SAED pattern displays diffused rings, consistent with a polycrystalline thin film (inset of Fig. 3b). Elemental mapping confirms a uniform distribution of Al, Co, Ni, Fe, and Mo across the film (Fig. 3c), with slight surface oxidation.

After dealloying, both samples are reconstructed into nanosheet arrays (Fig. 3d and S13). The nanosheets in D-Al_{32} are more uniform and better separated, giving a more open and porous surface that exposes more active area.[50] The cross-sectional TEM image shows that D-Al_{32} forms a thicker and more vertically aligned nanosheet layer, with a framework diameter of ~50 nm and a height above 100 nm (Fig. 3e). This oriented architecture provides straight transport pathways for electrolyte access and helps oxygen bubbles detach more easily. The HRTEM image of D-Al_{32} shows clear lattice fringes with a spacing of 0.2048 nm, matching the FCC (111) plane (Fig. 3f). The SAED rings are also sharper than those of D-$Al_{31.5}$, indicating higher structural order after reconstruction.[51] After the stability test, the D-Al_{32}/NF sample retained its vertically oriented nanosheet layer structure; in contrast, obvious nanosheet agglomeration persisted in the D-$Al_{31.5}$/NF sample (Fig. S14).

To ensure the accuracy of bubble-based screening, copper was initially adopted as the support. However, the resulting OER activity was relatively poor (Fig. S15). To enhance OER performance, nickel foam was used as the substrate instead, and systematic dealloying experiments with gradient durations were conducted. It was found that the optimal OER performance was achieved with a dealloying time of 1 h (Fig. S16). The OER polarization curves of Al_{32}/NF and $Al_{31.5}$/NF before and after dealloying are compared to highlight the catalytic performance, with bare Ni foam as a reference (Fig. 4a). Before dealloying, both alloy films show clear activity improvement over the Ni foam, confirming that introducing multicomponent metals enhances OER performance. Al_{32}/NF exhibits a lower onset potential and higher current response than $Al_{31.5}$/NF, which is consistent with the bubble-screening prediction that Al_{32} lies in the higher-activity region of the composition map. Al_{32}/NF requires an overpotential of 308 mV at 10 mA cm^{-2}, while $Al_{31.5}$/NF needs 326 mV under the same conditions. To further improve the catalytic activity, both samples were dealloyed in an alkaline solution, and their post-treatment performance is also shown in Fig. 4a. After dealloying, the

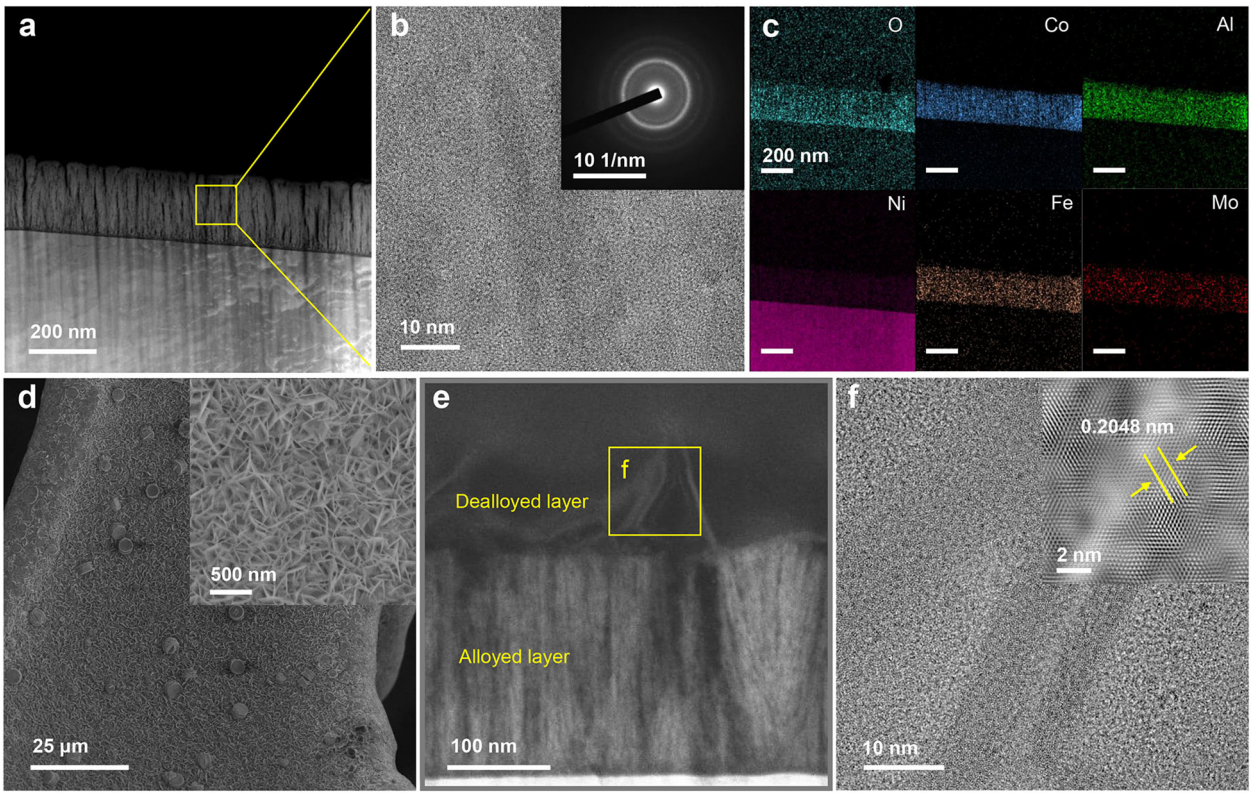

Fig. 3 Structural characterization of the Al_{32} sample before and after dealloying. (a) SEM image of the Al_{32} sample before dealloying. (b) HRTEM and SAED images of the Al_{32} sample before dealloying. (c) EDS image of the Al_{32} sample before dealloying. (d) SEM image of the Al_{32} sample after dealloying. (e) TEM image of the Al_{32} sample after dealloying. (f) HRTEM image of the Al_{32} sample after dealloying.

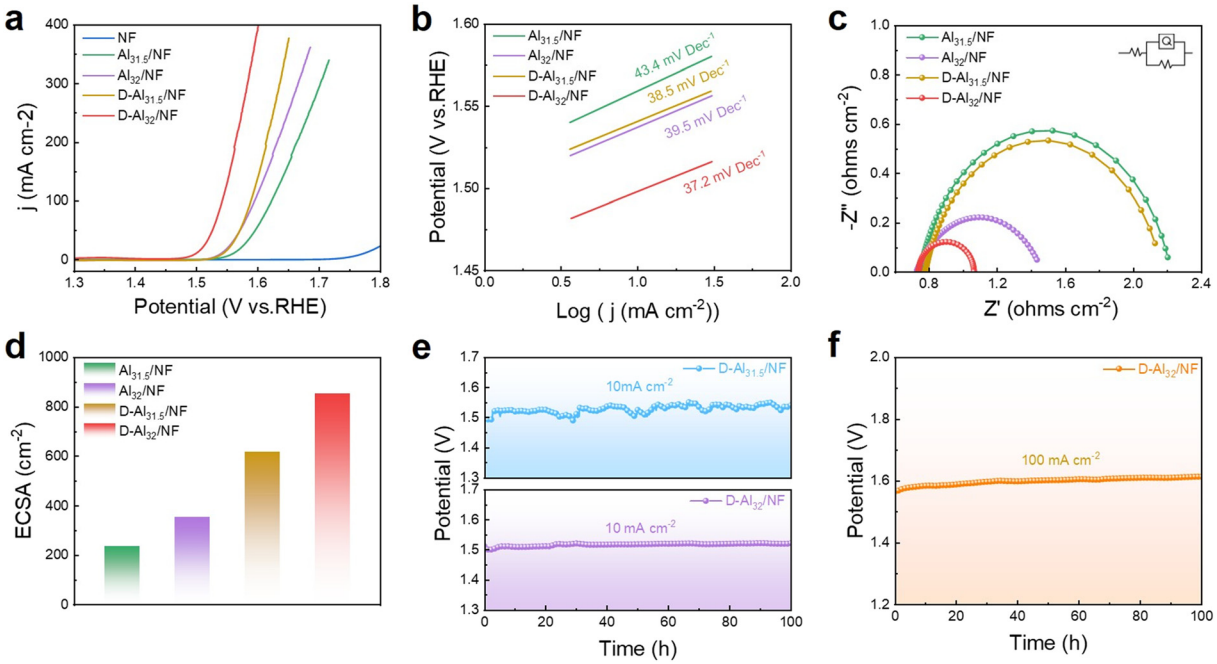

Fig. 4 (a) OER polarization curves. (b) Tafel slopes. (c) Nyquist plots. (d) ECSA comparison diagram. (e) Chronopotentiometric test at a current density of 10 mA cm^{-2}. (f) Long-term test at a current density of 100 mA cm^{-2}.

polarization curves shift to lower potentials for both compositions, indicating that dealloying activates the surface and improves OER kinetics. The improvement is stronger for Al_{32}. The dealloyed D-Al_{32}/NF reaches 269 mV at 10 mA cm^{-2} and 312 mV at 100 mA cm^{-2}, whereas D-$Al_{31.5}$/NF requires 312 mV at 10 mA cm^{-2} and a higher overpotential than D-Al_{32}/NF at 100 mA cm^{-2}. These results confirm that the composition selected from bubble screening remains optimal after reconstruction.[41] A comparison with recently reported advanced catalysts further shows that D-Al_{32}/NF falls among the leading performers in alkaline OER (Fig. S17).

After dealloying, D-Al_{32}/NF achieves a low Tafel slope of 37.1 mV dec^{-1}, which is smaller than that of D-$Al_{31.5}$/NF, indicating a more favorable kinetic response under the same electrolyte conditions (Fig. 4b). The impedance results show the same trend. In Fig. 4c, the Nyquist plots indicate that Al_{32}/NF has a smaller semicircle than $Al_{31.5}$/NF, and D-Al_{32}/NF shows the smallest semicircle after dealloying, which corresponds to the lowest charge-transfer resistance among the compared samples. To better understand whether the activity improvement is related to accessible active sites, we evaluated the electrochemical surface area change using double-layer capacitance extracted from CV scans (Fig. S18).[52] After dealloying, both compositions show a clear increase in capacitance, indicating a large increase in the accessible surface area caused by the reconstructed nanosheet structure. The increase is larger for Al_{32}, and D-Al_{32}/NF shows the highest ECSA among the samples (Fig. 4d). This result supports that dealloying exposes more active sites and improves electrolyte access, and it also explains why D-Al_{32}/NF delivers the highest current at the same potential.[53]

In the chronopotentiometric test at 10 mA cm^{-2} (Fig. 4e), D-Al_{32}/NF shows a smooth and stable potential profile, whereas D-$Al_{31.5}$/NF displays significant potential fluctuations. This behavior is consistent with their reconstructed morphologies. SEM and TEM images indicate that D-Al_{32}/NF forms a more uniform, vertically aligned nanosheet array with a more open porous network, while D-$Al_{31.5}$/NF shows more local aggregation and less ordered nanosheets. Such aggregated regions can lead to non-uniform gas-release pathways and local bubble trapping, which temporarily blocks active sites and increases local ohmic and charge-transfer resistance. The long-term test at 100 mA cm^{-2} confirms the durability of D-Al_{32}/NF. As shown in Fig. 4f, D-Al_{32}/NF maintains stable operation over 100 h, demonstrating that the reconstructed structure and the selected composition can sustain the OER under high current density.[54]

Fig. 5a shows the survey XPS spectra of Al_{32}/NF before and after dealloying. The pristine Al_{32}/NF displays clear Al, Co, Ni, Fe, Mo, and O signals. After dealloying, the Al signal is strongly suppressed, indicating that Al is largely removed from the near-surface region and acts as the sacrificial component that triggers surface reconstruction.[55–57] In the Co 2p spectra of pristine Al_{32}/NF (Fig. 5b), Co mainly appears as low-valence species with a noticeable metallic contribution, while the oxidized Co features are weaker. After dealloying, the Co 2p peaks shift to higher binding energies and the oxidized Co components become dominant. In typical fitting, Co^{3+}/Co^{2+} contributions appear in the Co $2p^{3/2}$

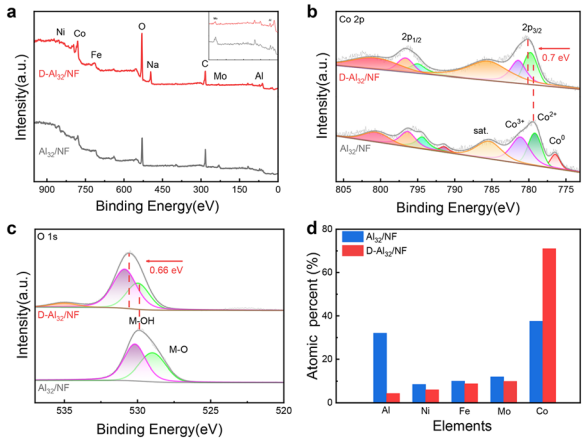

Fig. 5 (a) XPS survey spectra of Al_{32}/NF before and after dealloying. (b) Co 2p spectra. (c) O 1s spectra. (d) Surface atomic ratios of Al_{32}/NF before and after dealloying.

region around ~779.5–781.5 eV, which is consistent with the formation of Co(oxy)hydroxide-like species. The reduced metallic Co signal together with the enhanced high-valence Co features indicates that dealloying promotes surface oxidation and generates more Co^{3+}-rich active motifs.[53,58]

Compared with the pristine sample, the dealloyed surface exhibits a stronger contribution from oxidized oxygen species (Fig. 5c). The O 1s envelope can be assigned to metal–oxygen (M–O, typically ~529–530 eV) and hydroxyl oxygen (M–OH typically ~531–532 eV). The increased hydroxyl-related signal after dealloying supports the formation of an (oxy)hydroxide-rich surface layer, consistent with the nanosheet reconstruction observed by microscopy.[59–61] The surface atomic ratios before and after dealloying were quantified (Fig. 5d). The Co fraction increases strongly from ~37.5 at% in the pristine alloy to ~71 at% after dealloying, while the Al content drops from ~32 at% to <4.3 at%. This confirms a selective Al removal and Co enrichment process, which increases the density of Co-centered active sites at the reconstructed surface.[47,62]

The excellent OER performance of D-Al_{32}/NF arises from the coupled effects of dealloying-driven structure and electronic structure reconstruction. Efficient Al removal triggers a more complete structural reorganization, producing a uniform and vertically aligned nanosheet array as observed by SEM and cross-sectional TEM. This open architecture could increase electrolyte penetration and shorten transport pathways, which helps suppress local blockage during operation. At the same time, the reconstructed nanosheets markedly raise the accessible active-site density. These structural and chemical advantages translate into faster interfacial charge transfer, and they also explain the smoother potential response and higher stability compared with other multicomponent alloys.

Conclusions

In summary, this work demonstrates a practical route to design high-performance multicomponent alloy OER catalysts by combining composition-spread sputtering, bubble-based parallel screening, and dealloying activation. The bubble screening method rapidly links oxygen bubble evolution to local OER activity across a continuous composition gradient, allowing the fast identification of an optimal elemental ratio without testing each composition one by one. Guided by this screening, $Al_{32}Co_{37.5}Ni_{8.5}Fe_{10}Mo_{12}$ on Ni foam was selected and further improved by alkaline dealloying, which removed Al, enriched and oxidized Co at the surface, and reconstructed the film into vertically aligned nanosheet arrays, exhibiting impressive OER activities without noble metals. Overall, bubble screening offers a fast, intuitive strategy for multicomponent alloy catalyst discovery toward practical OER applications and holds great promise for extension to other gas-evolving reactions, demonstrating excellent potential for broad application.

Author contributions

Puchang Hou: data curation, software, validation, investigation, methodology, and writing – original draft; Ruizhe Ru: data curation methodology and writing – review & editing; Ziyong Zhang: data curation and formal analysis; Jinyan Xie: supervision and writing – review & editing; Lei Zhang: software and visualization; Fei Han: data curation and formal analysis; Guowei Li: conceptualization, funding acquisition, writing – review & editing, and resources; Juntao Huo: conceptualization, project administration, supervision, and writing – review & editing; Jun-Qiang Wang: conceptualization, supervision, writing – review & editing, funding acquisition, and resources.

Conflicts of interest

There are no conflicts to declare.

Data availability

The data supporting this article have been included as part of the supplementary information (SI).

Supplementary information: sample preparation, material characterization, electrochemical measurements, Fig. S1–S18, Table S1, and additional references. See DOI: https://doi.org/10.1039/d6cy00309e.

Acknowledgements

We acknowledge financial support from the National Natural Science Foundation of China (NSFC U24A2039 and 52471214), the Zhejiang Provincial Natural Science Foundation of China (Grant No. LRG26E010001), the Ningbo Yongjiang Talent Introduction Programme (2022A-090-G), the Yongjiang Talent Engineering Technology Innovation Team Project of Ningbo (No. 2022A-008-C), and the Zhejiang Provincial Natural Science Foundation of China (LR22E010004 and 2022C01023).

References

1 Y. Li, L. Zhou and S. Guo, *EnergyChem*, 2021, **3**, 100053.
2 Y.-C. Zhang, C. Han, J. Gao, L. Pan, J. Wu, X.-D. Zhu and J.-J. Zou, *ACS Catal.*, 2021, **11**, 12485–12509.
3 R. Jin, C. Yang, Z. Liu, J. Liu, S. Li, Y. Liu, K. Liu, R. Yin, J. Li and L. Gao, *Energy Environ. Mater.*, 2025, e70050.
4 Z. Zhang, B. Feng, J. Sun, G. Li, Z. Lu, J. Wang and J. Huo, *Small*, 2025, **21**, e01973.
5 Q. Jiang, S. Wang, C. Zhang, Z. Sheng, H. Zhang, R. Feng, Y. Ni, X. Tang, Y. Gu, X. Zhou, S. Lee, D. Zhang and F. Song, *Nat. Commun.*, 2023, **14**, 6826.
6 Q. Yu, Y. Chen, J. Liu, C. Li, J. Hu and X. Xu, *Proc. Natl. Acad. Sci. U. S. A.*, 2024, **121**, e2319894121.
7 S. Shen, Q. Li, H. Zhang, D. Yang, J. Gong, L. Gu, T. Gao and W. Zhong, *Adv. Mater.*, 2025, **37**, 2500595.
8 H.-Z. Wen, Y. Zhao, H.-T. Zhang, Z.-X. Wan-Me, X.-Y. Wan and Y.-L. Xie, *Catal. Sci. Technol.*, 2025, **15**, 3871–3877.
9 B. Hua, M. Li and J.-L. Luo, *Nano Energy*, 2018, **49**, 117–125.
10 W.-J. Yin, B. Weng, J. Ge, Q. Sun, Z. Li and Y. Yan, *Energy Environ. Sci.*, 2019, **12**, 442–462.
11 G. Li, S. Hou, L. Gui, F. Feng, D. Zhang, B. He and L. Zhao, *Appl. Catal., B*, 2019, **257**, 117919.
12 S. Liu, Y. Zhang, W. Sun, J. Wang, D. Zhang, J. Huo and G. Li, *Chem. Commun.*, 2025, **61**, 3669–3672.
13 Y. Kang, Y. He, D. Pohl, B. Rellinghaus, D. Chen, M. Schmidt, V. Süß, Q. Mu, F. Li, Q. Yang, H. Chen, Y. Ma, G. Auffermann, G. Li and C. Felser, *ACS Appl. Mater. Interfaces*, 2022, **14**, 19324–19331.
14 X. Hu, R. Wang, W. Feng, C. Xu and Z. Wei, *J. Energy Chem.*, 2023, **81**, 167–191.
15 Y. Ma, K. Siuzdak and G. Li, *Innovation Mater.*, 2025, **3**, 100157.
16 F. Chen, Z. Wu, Z. Adler and H. Wang, *Joule*, 2021, **5**, 1704–1731.
17 J. Guo, M. Zhou, Y. Shen, G. Yu, Q. Wang, H. Yu, L. Wang, F. Wang, W. Yang, H. Wang, Y. Ding, Y. Zhao and Z. Wang, *Energy Environ. Mater.*, 2026, e70261.
18 L. Wang, J. Li, Q. Meng, M. Xiao, C. Liu, W. Xing and J. Zhu, *Catal. Sci. Technol.*, 2024, **14**, 4166–4173.
19 Z. Zhu, Y. Lin, P. Fang, M. Wang, M. Zhu, X. Zhang, J. Liu, J. Hu and X. Xu, *Adv. Mater.*, 2023, **36**, 2307035.
20 L. Cai, J. Huo, P. Zou, G. Li, J. Liu, W. Xu, M. Gao, S. Zhang and J.-Q. Wang, *ACS Appl. Mater. Interfaces*, 2022, **14**, 15243–15249.
21 X. Shi, S. Sun, Y. Zhang, W. Sun, L. Wang, H. Li, K. Siuzdak and G. Li, *ChemCatChem*, 2025, **17**, e00494.
22 N. Lu, Y. Li, J. Wang, G. Li, G. Li, F. Liu and C. Y. Tang, *Mater. Horiz.*, 2025, **12**, 1944–1952.
23 M. Pan, H. Feng, Z. Zhang, M. Gao, L. Lei, D. Wang, G. Li, J. Huo and J.-Q. Wang, *J. Mater. Chem. A*, 2024, **12**, 15334–15342.
24 X. Zou, S. Zhi, B. Pang, X. Zhao, H. Ma, G. Zhao and H. Guo, *Energy Environ. Mater.*, 2025, **8**, e70057.
25 Q. Yang, Y. Zhang, Y. Sun, C. Felser and G. Li, *Innovation Mater.*, 2023, **1**, 100013.
26 S.-H. Chung, T. Li, T. Shoinkhorova, S. Komaty, A. Ramirez, I. Mukhambetov, E. Abou-Hamad, G. Shterk, S. Telalovic, A. Dikhtiarenko, B. Sirks, P. Lavrik, X. Tang, B. M. Weckhuysen, P. C. A. Bruijnincx, J. Gascon and J. Ruiz-Martínez, *Nat. Catal.*, 2023, **6**, 363–376.
27 Y. K. Kim, J. H. Kim, Y. H. Jo and J. S. Lee, *ACS Catal.*, 2019, **9**, 9650–9662.
28 Z. Fan, P. Zou, K. Jiang, W. Xu, M. Gao, V. Zadorozhnyy, G. Li, J. Huo and J.-Q. Wang, *Intermetallics*, 2023, **160**, 107946.
29 C. He, D. Pan, X. Li, Z. Lu, K. Chen, G. Wang, Z. Zhang, H. Zhang, Y. Zhang and Z. Wen, *Coord. Chem. Rev.*, 2025, **531**, 216496.
30 C. Li, X. Luo, Y. Wang, M. Zhu, D. Li, S. Guo, W. Wang and X. Xu, *Adv. Sci.*, 2025, **12**, e08013.
31 Z. Chen, C. Xu, F. Zhao, S. Xi, W. Li, M. Huang, B. Cai, M. Gu, H.-L. Wang and X. D. Xiang, *ACS Catal.*, 2022, **13**, 601–611.
32 T. A. A. Batchelor, T. Löffler, B. Xiao, O. A. Krysiak, V. Strotkötter, J. K. Pedersen, C. M. Clausen, A. Savan, Y. Li, W. Schuhmann, J. Rossmeisl and A. Ludwig, *Angew. Chem., Int. Ed.*, 2021, **60**, 6932–6937.
33 A.-E. Nieuwelink, J. C. Vollenbroek, R. M. Tiggelaar, J. G. Bomer, A. van den Berg, M. Odijk and B. M. Weckhuysen, *Nat. Catal.*, 2021, **4**, 1070–1079.
34 X. Wang, I. A. Cechanaviciute, L. Banko, S. Pokharel, T. Quast, A. Ludwig, O. Krysiak and W. Schuhmann, *Adv. Funct. Mater.*, 2024, **34**, 2400180.
35 A. Sanin, J. K. Flowers, T. H. Piotrowiak, F. Felsen, L. Merker, A. Ludwig, D. Bresser and H. S. Stein, *Adv. Energy Mater.*, 2025, **15**, 2404961.
36 R. Gutkowski, C. Khare, F. Conzuelo, Y. U. Kayran, A. Ludwig and W. Schuhmann, *Energy Environ. Sci.*, 2017, **10**, 1213–1221.
37 G. Xia, H. Yang, Z. Niu, L. Cui, G. Fu, Q. Wu and H. Zhi, *Renewable Sustainable Energy Rev.*, 2026, **225**, 116174.
38 Y. Zhang, K. E. Arpino, Q. Yang, N. Kikugawa, D. A. Sokolov, C. W. Hicks, J. Liu, C. Felser and G. Li, *Nat. Commun.*, 2022, **13**, 7784.
39 X. Liu, P. Zou, L. Song, B. Zang, B. Yao, W. Xu, F. Li, J. Schroers, J. Huo and J.-Q. Wang, *ACS Catal.*, 2022, **12**, 3789–3796.
40 P. Zou, L. Song, W. Xu, M. Gao, V. Zadorozhnyy, J. Huo and J.-Q. Wang, *J. Alloys Compd.*, 2023, **960**, 170656.
41 J. Hu, T. Guo, X. Zhong, J. Li, Y. Mei, C. Zhang, Y. Feng, M. Sun, L. Meng, Z. Wang, B. Huang, L. Zhang and Z. Wang, *Adv. Mater.*, 2024, **36**, 2310918.
42 Y. Chen, C. Guo, Y. Wang, K. Wang and S. Song, *Chin. J. Catal.*, 2025, **77**, 210–219.
43 D. Escalera-López, Y. Niu, S. J. Park, M. Isaacs, K. Wilson, R. E. Palmer and N. V. Rees, *Appl. Catal., B*, 2018, **235**, 84–91.
44 C. Huang, Y. Wang, L. Zhang, J. Huo, D. Ma, Q. Xu and G. Li, *Quantum Front.*, 2025, **4**, 19.
45 Z. Song, H. Min, M. Zhu, Y. Jiang, W. Luo, W. Wu, H. He, S. Nai, W. Wang, R. He, Q. Feng and Y. Jiang, *Adv. Funct. Mater.*, 2025, e23085.

46 Y. Li, X. Wang, C. Li, X. Han, S. Yin, J. Xia and H. Li, *Int. J. Hydrogen Energy*, 2024, **90**, 1041–1050.
47 W. Wang, L. Kuai, W. Cao, M. Huttula, S. Ollikkala, T. Ahopelto, A. P. Honkanen, S. Huotari, M. Yu and B. Geng, *Angew. Chem., Int. Ed.*, 2017, **56**, 14977–14981.
48 S. Park, L. Liu, Ç. Demirkır, O. van der Heijden, D. Lohse, D. Krug and M. T. M. Koper, *Nat. Chem.*, 2023, **15**, 1532–1540.
49 J. Yu, K. Hu, Z. Zhang, L. Luo, Y. Liu, D. Zhou, F. Wang, Y. Kuang, H. Xu, H. Li, H. Duan and X. Sun, *Energy Environ. Sci.*, 2023, **16**, 2068–2079.
50 S. Wang, P. Yang, X. Sun, H. Xing, J. Hu, P. Chen, Z. Cui, W. Zhu and Z. Ma, *Appl. Catal., B*, 2021, **297**, 120386.
51 C. C. Hou, L. Zou, Y. Wang and Q. Xu, *Angew. Chem., Int. Ed.*, 2020, **59**, 21360–21366.
52 Z. J. Chen, T. Zhang, X. Y. Gao, Y. J. Huang, X. H. Qin, Y. F. Wang, K. Zhao, X. Peng, C. Zhang, L. Liu, M. H. Zeng and H. B. Yu, *Adv. Mater.*, 2021, **33**, 2101845.
53 X. Zeng, Q. Zhang, C. Jin, H. Huang and Y. Gao, *Energy Environ. Mater.*, 2023, **7**, e12628.
54 J. Qi, Y. Xia, X. Meng, J. Li, S. Yang, H. Zou, Y. Ma, Y. Zhang, Y. Du, L. Zhang, Z. Lin and J. Qiu, *Adv. Mater.*, 2025, **37**, 2419058.
55 B. Liu, T. Lv, A. Zhou, X. Zhu, Z. Lin, T. Lin and L. Suo, *Nat. Commun.*, 2024, **15**, 2922.
56 Y. Liu, S. Niu, Y. Zou, S. Huang, Y. Shi, S. Gao and P. Tsiakaras, *Appl. Catal., B*, 2025, **363**, 124729.
57 Y. Chen, Q. Li, Y. Lin, J. Liu, J. Pan, J. Hu and X. Xu, *Nat. Commun.*, 2024, **15**, 7278.
58 X. Yu, J. Zhao and M. Johnsson, *Adv. Funct. Mater.*, 2021, **31**, 2101578.
59 H. Shi, X. Y. Sun, Y. Liu, S. P. Zeng, Q. H. Zhang, L. Gu, T. H. Wang, G. F. Han, Z. Wen, Q. R. Fang, X. Y. Lang and Q. Jiang, *Adv. Funct. Mater.*, 2023, **33**, 2214412.
60 L. Yang, L. Shi, H. Chen, X. Liang, B. Tian, K. Zhang, Y. Zou and X. Zou, *Adv. Mater.*, 2023, **35**, 2208539.
61 W. Huang, J. Li, X. Liao, R. Lu, C. Ling, X. Liu, J. Meng, L. Qu, M. Lin, X. Hong, X. Zhou, S. Liu, Y. Zhao, L. Zhou and L. Mai, *Adv. Mater.*, 2022, **34**, 2200270.
62 T. Jian, W. Ma, C. Xu, H. Liu and J. Wang, *eScience*, 2023, **3**, 100114.